

Numerical Study of Capillary Flow in Microchannels With Alternate Hydrophilic-Hydrophobic Bottom Wall

Auro Ashish Saha

Department of Mechanical Engineering,
Indian Institute of Technology, Bombay,
Mumbai 400076, India
e-mail: asaha@iitb.ac.in

Sushanta K. Mitra¹

Department of Mechanical Engineering,
University of Alberta,
Edmonton, AB T6G2G8, Canada
e-mail: sushanta.mitra@ualberta.ca

A two-dimensional numerical simulation of flow in patterned microchannel with alternate layers of different sizes of hydrophilic and hydrophobic surfaces at the bottom wall is conducted here. The effect of specified contact angle and working fluid (de-ionized (DI) water and ethanol) on capillary phenomena is observed here. The volume of fluid method is used for simulating the free surface flow in the microchannel. Meniscus profiles with varying amplitude and shapes are obtained under the different specified surface conditions. Nonsymmetric meniscus profiles are obtained by changing the contact angles of the hydrophilic and hydrophobic surfaces. A meniscus stretching parameter is defined here and its relation to the capillary phenomena in the microchannel is discussed. Flow variation increases as the fluid traverses alternately between the hydrophilic and hydrophobic regions. The pattern size and the surface tension of the fluid are found to have significant influence on the capillary phenomena in the patterned microchannel. Smaller pattern size produces enhanced capillary effect with DI water, whereas no appreciable gain is observed for ethanol. The magnitude of maximum velocity along the channel height varies considerably with the pattern size and the contact angle. Also, the rms velocity is found to be higher for smaller alternate patterned microchannel. The meniscus average velocity difference at the top and bottom walls increases for a dimensionless pattern size of 0.6 and thereafter it decreases with the increase in pattern size in the case of DI water with hydrophilic-hydrophobic pattern. Using such patterned microchannel, it is possible to manipulate and optimize fluid flow in microfluidic devices, which require enhanced mixing for performing biological reactions. [DOI: 10.1115/1.3129130]

Keywords: contact angle, capillary flow, microchannel, numerical, two-dimensional

1 Introduction

Manipulating gas and liquid flows within networks of microchannels is crucial in the design and fabrication of microfluidic devices. As the surface area to volume ratio increases, fluid/surface interactions become more significant with smaller fluidic channels [1]. Flow control is essential in many of the microfluidic systems targeted for use in biochemistry analysis, drug delivery, and sequencing or synthesis of nucleic acids, among others. Such systems use microchannels to promote efficient mixing without the use of any external means. These devices typically rely upon the balance of surface tension and fluid pressure forces to perform their function. When capillary action is used for microfluidics, the wetting property of microchannels has a significant effect on the liquid behavior. It is a well known fact that a hydrophilic surface assists fluid motion, whereas a hydrophobic surface retards fluid motion inside microchannels. It is thus possible to achieve flow control of liquid inside microchannels having differential wettability characteristics. Research on patterned surfaces reveal interesting phenomena that can be exploited to control liquid motions in microfluidic devices. Hydrophobic and hydrophilic regions inside microchannels can be patterned through surface modification. However, fabrication of such patterned surfaces with selective surface characteristics is highly challenging task [2].

There have been a few studies reported for flow in patterned microchannels. Zhao et al. [3] used surface directed liquid flow to

create pressure sensitive switches inside channel networks. Self-assembled monolayer chemistry is used in combination with multistream laminar flow and photolithography to pattern surface inside the microchannel networks. Kim et al. [4] carried out experimental and numerical investigation for microchannel transient filling process with surface tension. A linear relationship between the dimensionless pressure and capillary number is observed. Their experimental observations indicate that flow blockage in the narrowest width channel is enabled by the surface tension and not by viscous effect. Yang et al. [5] discussed the method to characterize the surface energy inside a microchannel by monitoring the marching velocity of capillary meniscus. They formulated one-dimensional mathematical model and performed experimental validation of liquid filling in a capillary. Parylene and silicon nitride microchannels, which are fabricated using surface micromachining technology, are used for experimentation. Their study indicates the influence of surface tension driven flow for fluid delivery in microfluidic systems.

Salamon et al. [6] used finite element based numerical method to study a three-dimensional flow of Newtonian fluid in a microchannel of height 80 μm with superhydrophobic lower and upper walls. They have shown a 40% flow enhancement over the smooth nonpatterned surface and an apparent slip length of 5.4 μm . Byun et al. [7] performed numerical visualization to investigate the effect of surface wettability in microchannel on the flow characteristics. The importance of hydrophobic and hydrophilic characteristics on a surface for the handling and control of liquid in the microsystems are emphasized. The study shows the occurrence of flow instability in the flow path when the meniscus crosses hydrophilic/hydrophobic interface. Dalton et al. [8] discussed is-

¹Corresponding author.

Contributed by the Fluids Engineering Division of ASME for publication in the JOURNAL OF FLUIDS ENGINEERING. Manuscript received June 10, 2008; final manuscript received April 1, 2009; published online May 13, 2009. Assoc. Editor: Rajat Mittal.

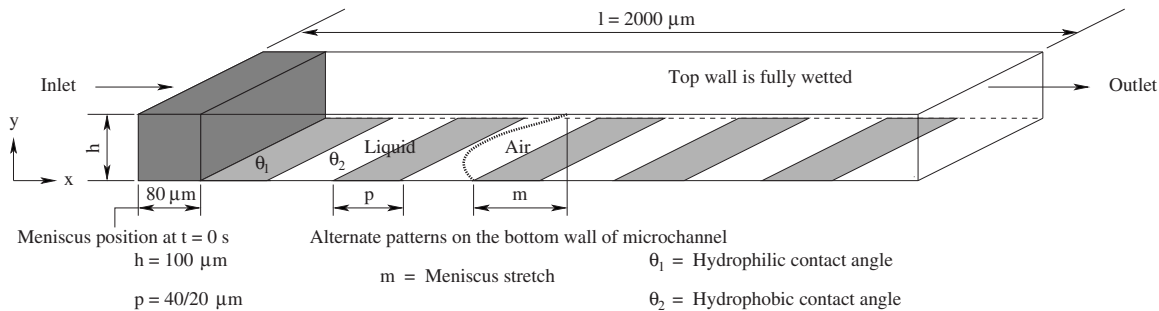


Fig. 1 Geometry of microchannel

sues in implementing superhydrophobic surfaces by nanostructured posts in a microchannel. The understanding and elimination of contact line movement effects on drag reduction are illustrated. Yang and Przekwas [9] developed the computational methodology to model surface tension effects of multifluid flow in ACE+MEMS CAD software. They present systematic validations against analytical solution for typical flows in microelectromechanical system (MEMS) devices. The unsteady motion of the free surface governed by the Hamilton–Jacobi evolution equation is solved on Eulerian grid using the volume of fluid (VOF) technique. Hirt and Nichols [10] described the concept of VOF method for treating complicated free boundary configurations. For simulation related to free surface flows, the water/air interface is characterized by surface tension and sharp changes in viscosity and density [11]. Among several general multiphase models currently in use, the VOF model has the ability to handle flows that undergo arbitrary topologic transformations [9]. Saha et al. [12] have used VOF method to study the capillary flow through microchannels with integrated pillars, which involved a complex flow geometry.

Huang et al. [13] studied theoretically and numerically the capillary filling flows inside patterned-surface microchannels: two different patterned microchannel configurations—inner walls patterned with unequal contact angles; each inner wall divided into two equal segments having different contact angles has been considered for carrying out two-dimensional and three-dimensional simulations. An equivalent contact angle model based on the surface energy method has been proposed for estimating capillary flows inside the patterned-surface microchannels and they validated the model with traditional capillary rise theories.

Recently, a new method has been developed to modify the hydrophobic and hydrophilic nature of silicon surfaces by the use of 5-(4-hydroxyphenyl)-10, 15, 20-tetra(*p*-tolyl) porphyrin self-assembled monolayer (SAM) [14]. The bare SiO₂ substrate exhibited a contact angle of 33 deg ± 2 deg showing hydrophilic nature of the surface. In the case of hydroxy-phenyl porphyrin SAM, the contact angle is found to increase up to 75 deg ± 3 deg, indicating a hydrophobic nature of the surface due to the formation of SAM on the SiO₂ surface. Until now, the studies have considered patterned surfaces that are uniform about the channel axis. In this present study, we deviate from the above restriction and study the surface dominated flow behavior in a channel with nonuniform distribution of surface characteristics with respect to channel axis. A two-dimensional numerical simulation of flow in patterned microchannels with alternate hydrophilic and hydrophobic surfaces at the bottom wall is presented. The hydrophilic surface induces the acute static contact angle, while the hydrophobic surface results in the obtuse static contact angle. The capillary driven flow phenomena in the microchannel is considered in this study. Capillary driven flows are purely governed by the forces associated with surface tension [15] and offer positive flow enhancement effect. To the best of the authors' knowledge, numerical investigation of alternate patterned microchannel with hydrophilic-hydrophobic bottom wall has not been reported so far, which accounts for the different working fluids, pattern size, and

variation in the surface wettability of the patterns. The results obtained from simulations also provide the required motivation for fabricating such patterned microfluidic device.

2 Physical Problem

The geometry of the microchannel model is shown in Fig. 1. The channel considered here is a two-dimensional channel with the channel dimension perpendicular to the plane of the figure much larger than the channel height in *y*-coordinate direction. The height *h* of the channel is 100 μm. The model consists of a single straight segment of 2000 μm in length. The alternate patterns of hydrophilic and hydrophobic surface arrangement are shown at the bottom wall of the channel geometry, to account for the surface tension and wall adhesion effects on the flow. Two types of microchannel geometry with 40 μm and 20 μm pattern sizes (*p*), respectively, are considered here.

2.1 Governing Equations. Equations for numerical (VOF model) and analytical (Lucas–Washburn and reduced order model) solutions for the propagation of a liquid in a channel is presented in Secs. 2.1.1–2.1.3.

2.1.1 VOF Model. The simulations of the capillary flows in the patterned-surface microchannels are performed using a VOF method. In this method, a volume fraction transport equation is employed in addition to the continuity and momentum equations. Two phases (gas-liquid) are treated as a homogeneous gas-liquid mixture. The flow is considered to be laminar, nongravity, incompressible, Newtonian, and isothermal with velocity field **V** and governed by the Navier–Stokes and continuity equations, as provided here:

$$\nabla \cdot \mathbf{V} = 0 \quad (1)$$

$$\frac{\partial \rho \mathbf{V}}{\partial t} + \nabla \cdot (\rho \mathbf{V} \mathbf{V}) = -\nabla P + \nabla \cdot (\mu (\nabla \mathbf{V} + \nabla^T \mathbf{V})) + \mathbf{F}_s \quad (2)$$

where **V** is the velocity of the mixture, *P* is the pressure, *t* is the time, **F_s** is the volumetric force at the interface resulting from surface tension, and ρ and μ are the density and viscosity, respectively. In this equation, the accumulation and convective momentum terms in every control volume (cell) balance the pressure force, shear force, and additional surface tension force **F_s**. Surface tension arises as a result of attractive forces between molecules in a fluid and it is represented as force acting only at the surface, which is required to maintain equilibrium in such instances.

The numerical simulation of free surface flows composed of two immiscible fluids involves two coupled tasks, namely, resolving the flow field and updating the position of the interface. This involves the application of SIMPLE algorithm [16] and extending it to include the VOF methodology [10,11]. The VOF method allows for the simulation of a mixture of two incompressible and immiscible fluids including surface tension effects. The VOF model includes the effects of surface tension along the interface between each pair of phases. The model can be augmented by the

additional specification of the contact angles between the phases and the walls. The fluids under consideration are DI water and ethanol as liquids and air as gas. The tracking of the interfaces between the phases is accomplished by the solution of a continuity equation for the volume fraction of any of the phases. The fields for all variables and properties are shared by the phases and represent volume-averaged values, as long as the volume fraction of each of the phases is known at each location. Thus the variables and properties in any given cell either represent one or a mixture of the phases, depending on the volume fraction values. The distribution of the liquid phase is described by using a single scalar field variable, F , which defines the fraction of the liquid volume. Here, $F=1$ represents liquid, $F=0$ represents gas, and $0 < F < 1$ represents the liquid/gas interface. The volume fraction distribution can be determined by solving the passive transport equation, given as

$$\frac{\partial F}{\partial t} + \mathbf{V} \cdot \nabla F = 0 \quad (3)$$

where

$$F = \frac{\text{cell volume occupied by liquid}}{\text{total volume of the control cell}} \quad (4)$$

The mixture's physical properties are derived from that of the two phases through the volume fraction function. In particular, the average value of ρ and μ in a computational cell can be computed from the value of F in accordance with

$$\rho = F\rho_2 + (1 - F)\rho_1 \quad (5)$$

$$\mu = F\mu_2 + (1 - F)\mu_1 \quad (6)$$

where the subscripts 1 and 2 represent the gas phase and the liquid phase, respectively.

The surface tension model follows the continuum surface force (CSF) model proposed by Brackbill et al. [17]. The surface tension is specified as a source term \mathbf{F}_s in Eq. (2) according to the CSF model:

$$\mathbf{F}_s = \sigma \kappa \nabla F \quad (7)$$

The surface tension is taken to be constant along the surface and only the forces normal to the interface are considered. According to the CSF model, the surface curvature κ is computed from local gradients in the surface normal to the interface, which is given as

$$\kappa = \frac{1}{|\mathbf{n}|} \left(\left(\frac{\mathbf{n}}{|\mathbf{n}|} \cdot \nabla \right) |\mathbf{n}| - \nabla \cdot \mathbf{n} \right) \quad (8)$$

where $\mathbf{n} = \nabla F$ is the normal vector. Wall adhesion is included in the model through the contact angle:

$$\hat{\mathbf{n}} = \hat{\mathbf{n}}_w \cos \theta + \hat{\mathbf{t}}_w \sin \theta \quad (9)$$

where $\hat{\mathbf{n}}$ is the unit vector normal to the surface, $\hat{\mathbf{n}} = \mathbf{n}/|\mathbf{n}|$, and $\hat{\mathbf{n}}_w$ and $\hat{\mathbf{t}}_w$ represent the unit vector normal and tangent to the wall, respectively. It may be noted that the code calculates only the macroscopic effects of surface tension and just tracks the interface progression under this force; it does not impose the specified contact angle to the interface at the wall. The interface needs to be constructed based on the computed value of the volume fraction with the application of interpolation schemes for the identification of the interface. An upwind scheme with the piecewise linear interface construction (PLIC) method is adopted for surface reconstruction [11]. In the PLIC scheme, the liquid-gas interface is assumed to be linear and can take any orientation within the cell. The reconstructed interface is represented by line segments in a two-dimensional flow. The reconstruction is required at every time step to include the necessary backcoupling of surface forces to the momentum equations, as well as flux calculations. Equations (1)–(9) are solved iteratively to obtain the liquid volume fraction

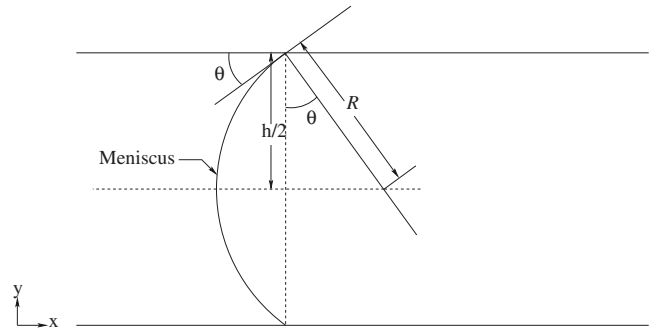


Fig. 2 Meniscus in channel in front view

and the velocity field solution under appropriate initial and boundary conditions. No slip boundary conditions at the walls are imposed. However, this will not restrict the contact line at wall from moving, as the code integrates over the whole cell adjacent to the wall to compute the mass flux of the second phase, which, when using finite grid size, will average out to give an apparent finite interface velocity at the wall [18]. As an initial condition, a distribution of F in the microchannel needs to be specified.

2.1.2 Lucas–Washburn Model. For a fully developed capillary driven flow, the balance of viscous force, surface tension force, and gravitational force yields the classical Lucas–Washburn equation, which relates the distance traveled by the liquid meniscus L with time t [19]. The analytical solution is based on the Navier–Stokes equation for incompressible, quasi-steady, laminar, non-gravity, Newtonian unidirectional horizontal flow for a two-dimensional channel:

$$-\frac{\partial P}{\partial x} = -\mu \frac{\partial^2 u}{\partial y^2} \quad (10)$$

where P is the pressure in the fluid at x , μ is the viscosity of the fluid, and u is the velocity of the fluid.

For static wetting of a liquid between two surfaces, the minimization of surface area of a liquid may result in a curved interface. The general Young–Laplace equation describes the relation for the pressure difference across the interface as

$$\Delta P = \sigma \left(\frac{1}{R_1} + \frac{1}{R_2} \right) \quad (11)$$

where ΔP is the pressure difference, σ is the liquid surface tension, and R_1 and R_2 are the radii of curvature of the interface in directions perpendicular and parallel to the liquid stream. For a two-dimensional channel $R_2 = \infty$.

Therefore Eq. (11) reduces to

$$\Delta P = \sigma \frac{1}{R} \quad (12)$$

Figure 2 shows the meniscus profile in a two-dimensional channel. Here, from Fig. 2,

$$R = \frac{h}{2 \cos \theta} \quad (13)$$

For steady two-dimensional Poiseuille flow, the average fluid velocity within the microchannel can be written as

$$u_{\text{avg}} = \frac{1}{12\mu} \frac{\Delta P}{L} h^2 \quad (14)$$

which can be related to the distance traveled by the liquid meniscus as

$$u_{\text{avg}} = \frac{dL}{dt} \quad (15)$$

Table 1 Boundary conditions for Cases 1 and 2

Case	Surface type	Boundary conditions on bottom wall
Case 1	Alternate hydrophilic-hydrophobic	Contact angles $\theta_1=30$ deg and $\theta_2=120$ deg
Case 2	Alternate hydrophilic-neutral	Contact angles $\theta_1=0$ deg and $\theta_2=90$ deg

Hence, the distance traveled by the liquid meniscus can be written as

$$L = \left(\frac{ht\sigma \cos \theta}{3\mu} \right)^{1/2} \quad (16)$$

Equation (16) shows that the flow time is inversely proportional to the surface tension, channel height, and the cosine of the wetting angle (θ), and directly proportional to the viscosity and the square of the flow distance.

2.1.3 Reduced Order Model. With quasisteady state assumption in the Lucas–Washburn model, the term denoting the momentum change in Navier–Stokes equation is often omitted [20]. For a microscale flow, the Reynolds number is usually very small and the surface tension force is always dominant. The quasisteady state assumption is valid except for the initial starting stage that is highly transient. In the reduced-order model, a transient solution is derived accounting for the momentum change, which is obtained by averaging the Navier–Stokes equations across the liquid length in the microchannel.

The momentum conservation may be expressed as the momentum change is balanced by the sum of the surface tension force, pressure overhead, and wall viscous force. At time t , L is the distance traveled by the liquid meniscus, u_{avg} is the average fluid velocity, and the momentum balance can be written as

$$\frac{d}{dt}(\rho h L u_{\text{avg}}) = 2\sigma \cos \theta + \Delta P h - \frac{12\mu L}{h} u_{\text{avg}} \quad (17)$$

For a passive capillary filling process, $\Delta P=0$. Noting $u_{\text{avg}} = dL/dt$, the equation above can be rewritten as

$$\frac{d^2}{dt^2} L^2 + B \frac{d}{dt} L^2 = A \quad (18)$$

where

$$A = \frac{4\sigma \cos \theta + 2\Delta P h}{\rho h}, \quad B = \frac{12\mu}{\rho h^2} \quad (19)$$

Considering initially the liquid meniscus position in the channel as L_0 and with zero velocity, the transient solution of the capillary filling problem is given as

$$L = \left(\frac{A}{B^2} \exp(-Bt) + \frac{At}{B} + \left(L_0^2 - \frac{A}{B^2} \right) \right)^{1/2} \quad (20)$$

$$u_{\text{avg}} = \frac{A(1 - \exp(-Bt))}{2BL} \quad (21)$$

where t is the time of the filling process, L is the distance traveled by the liquid meniscus, and u_{avg} is the average filling speed.

For the channel height of $100 \mu\text{m}$ selected in this study, the Bond number (Bo), $\rho g H^2 / \sigma$, and Capillary number (Ca), $\mu U / \sigma$, are much less than unity. The contact angle dependence on the speed of the contact line will be less pronounced here [21]. Hence, the effects of gravity and dynamic contact angle are not taken into account in the present study. The research on the dynamics of capillary phenomena and their applications has been reviewed in Refs. [21–24].

2.2 Initial and Boundary Conditions. Initially, at time $t=0$, the liquid meniscus position in the channel is set as $80 \mu\text{m}$, which is assumed to be flat. No slip boundary condition is imposed on all

the walls and the boundary conditions for the surface affinity is described by the contact angle. The contact angle specified on the bottom walls of the channel is shown in Fig. 1 and summarized in Table 1 for easy reference. The top wall is considered to be fully wetted with a contact angle of 0 deg. At the bottom wall, the initial meniscus position kept at $80 \mu\text{m}$ from the inlet is also considered as fully wet. Passive capillary filling process is considered for all the cases by specifying a constant pressure (atmospheric) at channel inlet and outlet. Liquid volume fraction values of unity and zero is specified at channel inlet and outlet, respectively, for all the cases.

3 Numerical Technique

The channel geometry is created and meshed using preprocessor CFD-GEOM modeler [25]. Structured grid having $2000(10 \times 200)$ square cells is used for simulations. The choice of such grid size is discussed in details in Sec. 4. CFD software CFD-ACE+ based on finite volume method is used for the time dependent simulations. Flow and free surface (VOF) modules of CFD-ACE+ are used for analysis. Second-order PLIC surface reconstruction method with surface tension effect is specified for VOF with explicit time integration scheme. Explicit option is selected as it exhibits greater stability and better convergence but slightly lower accuracy as compared with the implicit scheme. However, for an accurate resolution of the interface and prediction of the interface shape and its location, this is the preferred option. Euler (first-order) scheme is applied for time accuracy. A target Courant–Friedrich–Lewy ($\text{CFL} = |v| \delta t / h$) number of 0.1 is applied for numerical stability of the simulation. This would allow the interface to cross 10% of the width of a grid cell during each time step in a VOF computation. Upwind scheme is used for spatial differencing. Semi-implicit method for pressure-linked equation consistent (SIMPLEC) algorithm is adopted for pressure-velocity coupling and pressure correction. The conjugate gradient squared plus preconditioning (cgs+Pre) solver [25] is used for velocity, while the algebraic multigrid (AMG) solver is used for pressure correction. An initial time step of 1.0×10^{-7} s is selected and the VOF module is allowed to automatically adjust the time-step size based on the CFL number and interface velocity. An automatic time-step option automatically ensures stability in the CFD-ACE+ solver. Each case is given 100 iterations per time step with a convergence criteria of 0.0001 to control the iterative solution process. The solver quits the iterative procedure when the maximum relative difference between the computed values of variables in two successive iterations is smaller than the specified convergence criteria. The physical properties of DI water and ethanol used for simulations are provided in Table 2.

Table 2 Fluid properties used in simulation

Physical property	DI water	Ethanol	Air
Density (kg/m^3)	1000	791	1.1614
Viscosity (Pa s)	1.0×10^{-3}	1.2×10^{-3}	1.846×10^{-5}
Surface tension (N/m)	72.5×10^{-3}	21.38×10^{-3}	-

4 Results and Discussion

4.1 Validation of Model. Validation of the numerical results with analytical solution has been carried out for nonpatterned microchannel 100 μm height and 2000 μm length with contact angle $\theta=45$ deg for DI water. The time evolution of meniscus displacement is considered as the parameter for validating the numerical results. Figure 3(a) shows the comparison of meniscus displacement obtained numerically with the analytical solution based on a reduced-order model [20]. Good agreement between numerical and analytical results is observed. It is to be noted that, in general, the meniscus displacement in a capillary follows the Lucas–Washburn equation, which predicts that the distance traveled by the meniscus is proportional to \sqrt{t} . The Lucas–Washburn equation is an asymptotic model for large times and is derived based on the balance of capillary and friction forces when the influence of other forces during the initial transients becomes insignificant [26]. This quasisteady state assumption is valid except for the initial starting stage, which is highly transient. The validation studies reported in literature [5,9,13] are observed for very large time scale ($t \sim \text{s}$). However, the time scale considered for the present study is in the range of milliseconds ($t \sim \text{ms}$) for all the cases. Therefore, the plots in Fig. 3(a) do not necessarily obey the Lucas–Washburn equation, but a reduced-order model [20], which accounts for the inertia, is found to be a better choice for the representation of the meniscus displacement under the given con-

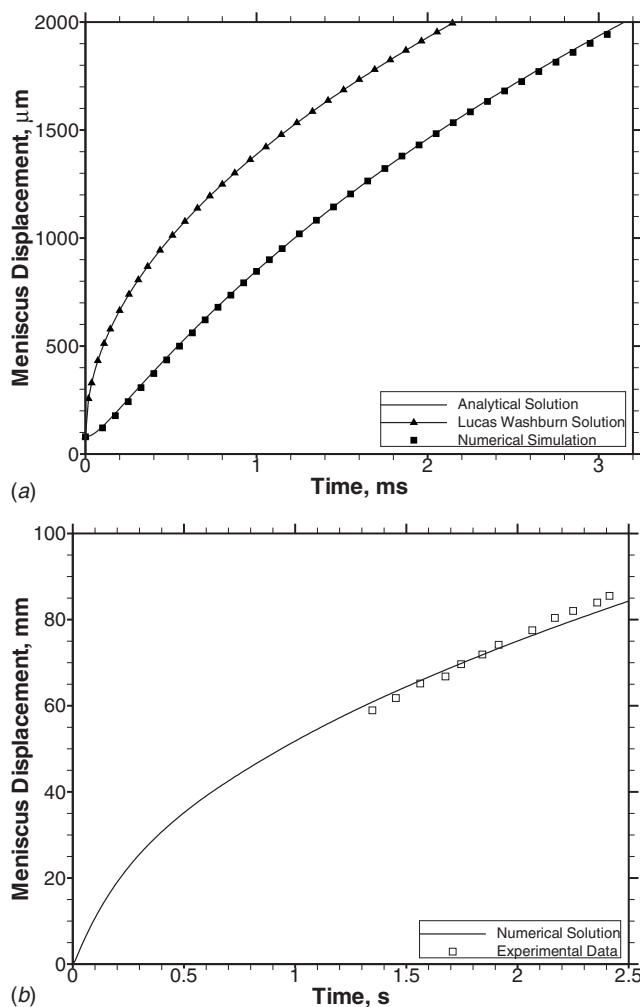


Fig. 3 Validation of numerical model with analytical solution [20] and experimental data [27]: (a) Verification with analytical solution and (b) verification with experimental data

ditions. Hence, deviation between the predicted numerical results and the Lucas–Washburn model can be justified. To demonstrate this, the numerical results are also validated with experimental data [27]. The geometry considered is a two-dimensional microchannel 1 mm height and 100 mm length with contact angle $\theta = 0$ deg. The liquid used in the experimental data is FC-77 with the following physical properties: the density $\rho = 1789 \text{ kg/m}^3$, the viscosity $\mu = 0.01548 \text{ Pa s}$, and the surface tension $\sigma = 0.015 \text{ N/m}$. Figure 3(b) shows the comparison of meniscus displacement obtained numerically with the experimental data. The numerical results again show good agreement with the experimental data. As the experimental data are available for a long time, we also observe that the meniscus displacement follows the Lucas–Washburn equation and is proportional to \sqrt{t} within the experimental time domain.

4.2 Snapshot of Meniscus Front. Figure 4 shows the snapshot images of the meniscus front in the microchannel for Case 1 with alternate hydrophilic–hydrophobic bottom wall when the microchannel is 25%, 50%, 75%, and 90% filled. The vertical line indicates an initial liquid meniscus position at 80 μm from the channel inlet. The isocontour of $F=0.5$ is applied to identify the interfacial position for the visualization. A nonsymmetric meniscus shape is observed during the capillary flow due to the alternate contact angle ($\theta_1 = 30$ deg, $\theta_2 = 120$ deg) specified on the bottom wall. Appreciable differences in the front shapes are observed between 40 μm and 20 μm pattern geometries for both DI water and ethanol. The meniscus shapes for Case 2 with alternate hydrophilic–neutral bottom wall, as shown in Fig. 5, is also found to be nonsymmetric about the channel axis. The meniscus curvature for Case 1 is observed to be larger compared with Case 2. This is due to pronounced retarding flow effect on the bottom wall and stretching of the meniscus on the top wall. Hence Figs. 4 and 5 show that the meniscus profiles vary in amplitude and shape when alternate patterns are produced in the microchannel.

4.3 Meniscus Stretch. The nonuniform distribution of surface characteristics with respect to channel axis results in the stretching of the meniscus in the microchannel. A meniscus stretch parameter is defined for this purpose, as illustrated in Fig. 1. The meniscus stretch is defined as the difference of the x -coordinate of the meniscus front on the top and bottom walls. Figure 6 shows the variation of meniscus stretch with liquid volume fraction for Cases 1 and 2.

The meniscus stretch is observed to fluctuate with liquid volume fraction for Cases 1 and 2. The meniscus stretch for Case 1 is large compared with Case 2 for both DI water and ethanol. The pattern size and the specified surface condition are seen to have significant effect on the amplitude and frequency of fluctuation of meniscus stretch parameter. To this respect, the meniscus stretch is also plotted for nonpatterned surfaces in Fig. 7, which shows that a highly hydrophobic bottom wall ($\theta = 120$ deg) causes a large meniscus stretch and a constant meniscus stretch of zero is found for fully wet walls. Therefore, it can be concluded that compared with the alternate pattern considered for Case 2 the alternate pattern for Case 1 offers higher hydrophobicity on the bottom wall. Compared with 20 μm patterned walls for both DI water and ethanol, the amplitude for Cases 1 and 2 is observed to be slightly higher for 40 μm patterned walls. The frequency of fluctuation is proportional to the number of patterns on the bottom wall. This also has its corresponding effect on the amplitude as the large number of patterns of smaller size tends to make the bottom wall less hydrophobic. This is reflected very clearly for 20 μm patterned wall, which has double the number of patterns than 40 μm patterned wall. Such effect is more pronounced with DI water than compared with ethanol.

4.4 Meniscus Displacement. The position of capillary meniscus for Cases 1 and 2 is shown in Fig. 8. As the meniscus shape is spatially distributed with respect to the x - and y -coordinate direc-

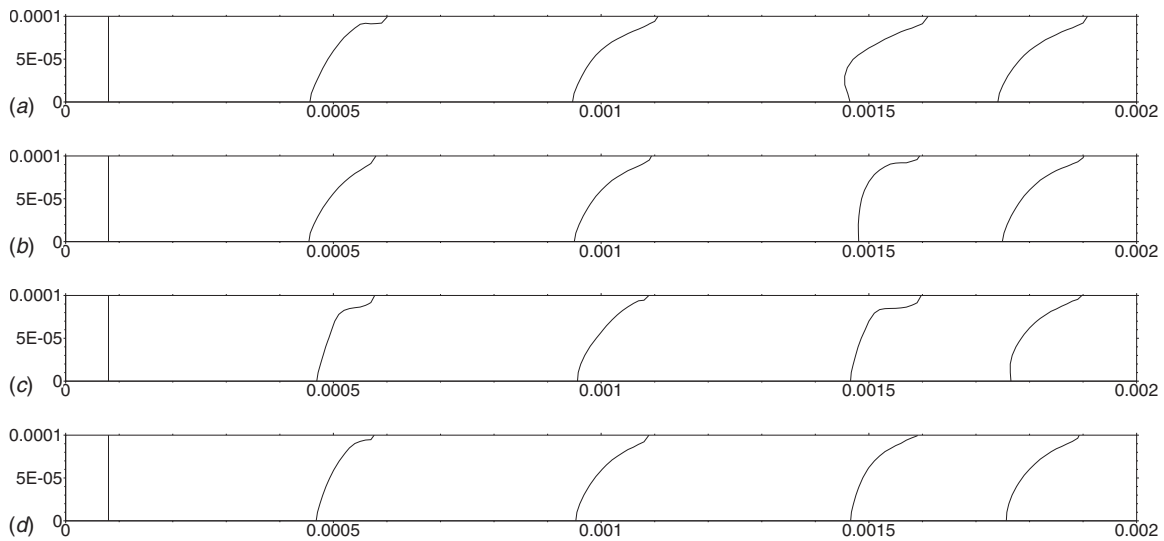


Fig. 4 The snapshot image of the evolution of meniscus front for Case 1 ($\theta_1=30$ deg, $\theta_2=120$ deg) when the microchannel is 25%, 50%, 75%, and 90% filled (isocontour of $F=0.5$ is applied to identify the meniscus): (a) DI water with $40 \mu\text{m}$ alternate pattern; (b) ethanol with $40 \mu\text{m}$ alternate pattern; (c) DI water with $20 \mu\text{m}$ alternate pattern; and (d) ethanol with $20 \mu\text{m}$ alternate pattern

tions and varies considerably for all the cases, the capillary meniscus position has been normalized with respect to the x -coordinate distance [13]. The normalized capillary meniscus position is obtained by dividing the volume of the fluid in the capillary with the height of the microchannel. It is observed that the capillary driven flow produces a nonlinear displacement of the meniscus. It is found that the meniscus displacement for alternate hydrophilic-hydrophobic condition (Case 1) is lower than the hydrophilic-neutral condition (Case 2) for both DI water and ethanol, whereas the displacement magnitude is lower for ethanol. It is to be noted that the detail displacement within the initial milliseconds is shown in the inset plot, which suggests that under different surface conditions, the transient response of the meniscus displacement varies significantly. Even such response propagates at a later time instant, as shown in Table 3.

The influence of contact angle on the meniscus displacement can be observed in Fig. 9, which is obtained for nonpatterned

surfaces. However, as shown in Fig. 8, the meniscus displacement for the alternate patterned microchannel (Case 1) is somewhat average of the corresponding nonpatterned surfaces with contact angles 30 deg and 120 deg, respectively, as shown in Fig. 9. The meniscus displacement may be manipulated suitably by appropriate choice of pattern size and surface contact angle, as shown in Fig. 8. In Fig. 8(a), it is observed that with DI water, for Cases 1 and 2, the microchannel with $20 \mu\text{m}$ patterned wall has large meniscus displacement compared with the $40 \mu\text{m}$ patterned wall. However, ethanol, having higher viscosity and lower surface tension compared with DI water, do not show pronounced difference in its meniscus displacement for patterned walls (Fig. 8(b)) for Cases 1 and 2.

4.5 Meniscus Instantaneous Velocity Distribution. Figure 10 shows the displacement of the capillary meniscus with time on the bottom wall with DI water (contact angles $\theta_1=30$ deg and

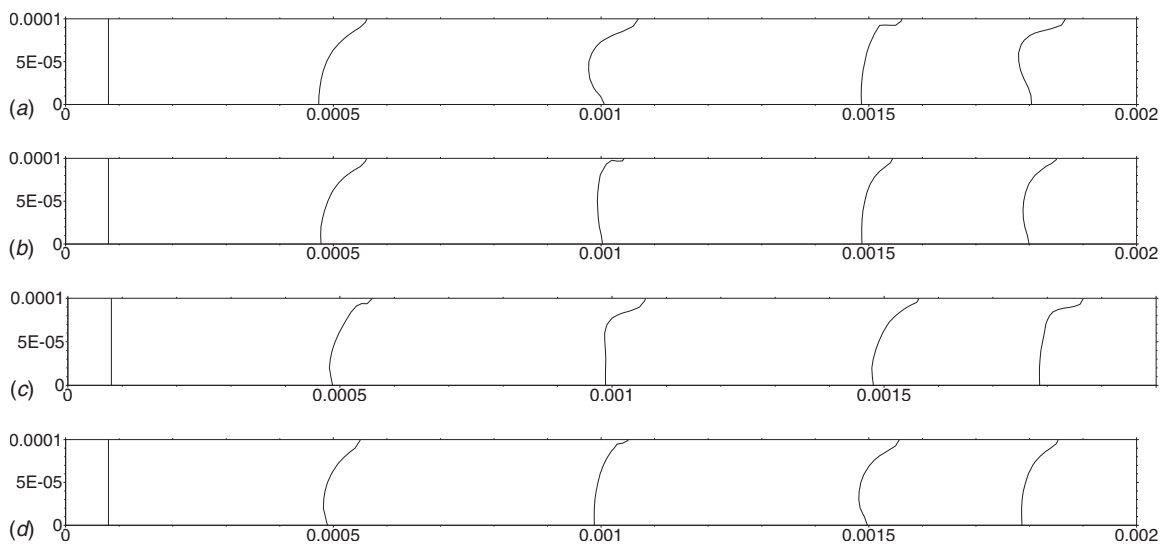
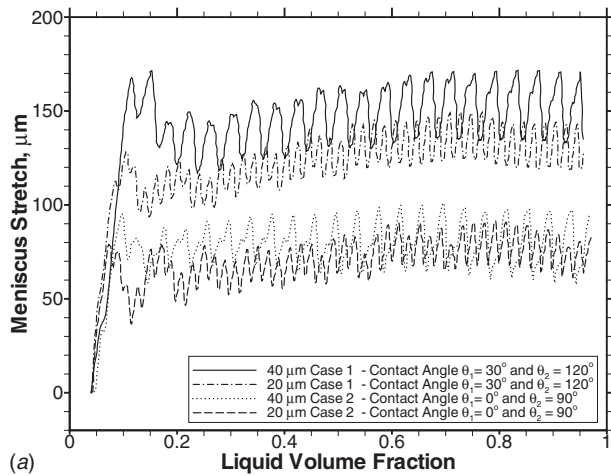
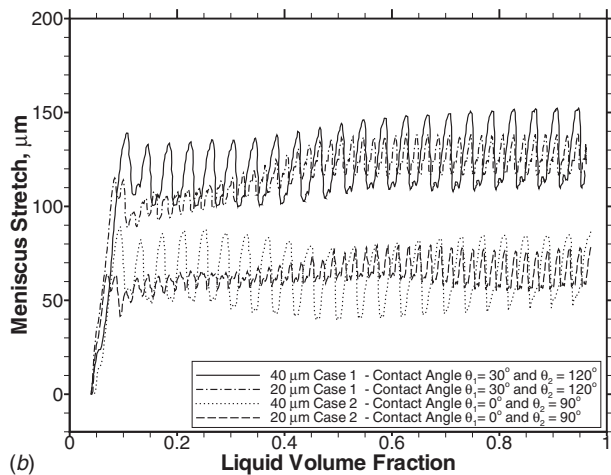


Fig. 5 The snapshot image of the evolution of meniscus front for Case 2 ($\theta_1=0$ deg, $\theta_2=90$ deg) when the microchannel is 25%, 50%, 75%, and 90% filled (isocontour of $F=0.5$ is applied to identify the meniscus): (a) DI water with $40 \mu\text{m}$ alternate pattern; (b) ethanol with $40 \mu\text{m}$ alternate pattern; (c) DI water with $20 \mu\text{m}$ alternate pattern; and (d) ethanol with $20 \mu\text{m}$ alternate pattern



(a)

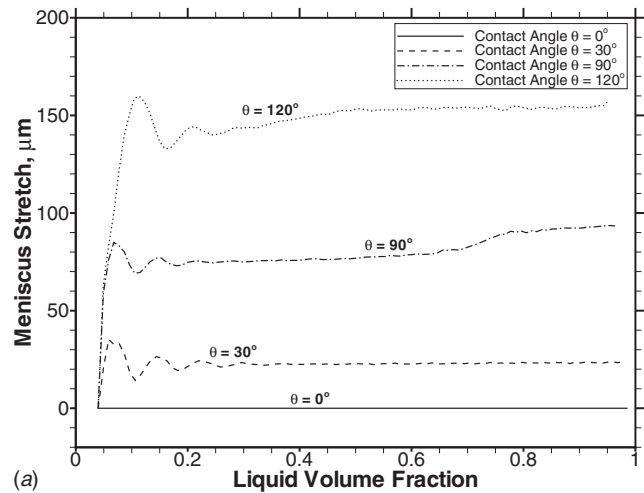


(b)

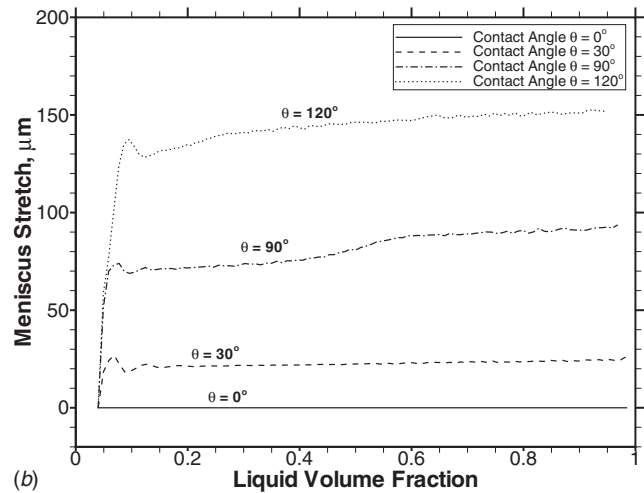
Fig. 6 The variation of meniscus stretch with liquid volume fraction for Cases 1 and 2 for two different working fluids: (a) DI water and (b) ethanol

$\theta_2=120$ deg) for 20 μm and 40 μm patterned microchannels. The velocity of the advancing meniscus is also plotted in Fig. 10. The velocity of the advancing liquid front at x -position is obtained by the derivative of the liquid front position with time at $\text{time}=t$. The hydrophilic and hydrophobic regions have been marked in the plot. It is observed that the velocity of the meniscus increases/decreases when the flow reaches the hydrophilic/hydrophobic interface region on the bottom wall.

Figure 11 shows the instantaneous velocity distribution along the channel height for Cases 1 and 2 when the microchannel is 50% filled. The meniscus velocity magnitudes are observed to be higher for DI water compared with ethanol for all the cases including the 40 μm and 20 μm patterned walls. As the fluid at the bottom wall traverses alternately from hydrophilic region to hydrophobic region, the curvature of the meniscus changes very sharply and large velocity gradients are observed at the wall for Cases 1 and 2. The gradients are observed to be higher for the 20 μm patterned wall compared with the 40 μm patterned wall (Fig. 10) and also the velocity magnitude values for Case 2 is higher compared with Case 1 for both DI water and ethanol. This is due to the higher hydrophilic nature of the bottom wall in Case 2 compared with Case 1. Additionally, the smaller pattern size (20 μm patterned wall) also tends to add additional hydrophilic effect in the microchannel. Overall, this results in flow variations in the microchannel. Such flow variations will be absent in the case of nonpatterned microchannel. The position of the maximum velocity magnitude along the channel height varies considerably for all the cases. It is therefore possible to manipulate fluid flow



(a)

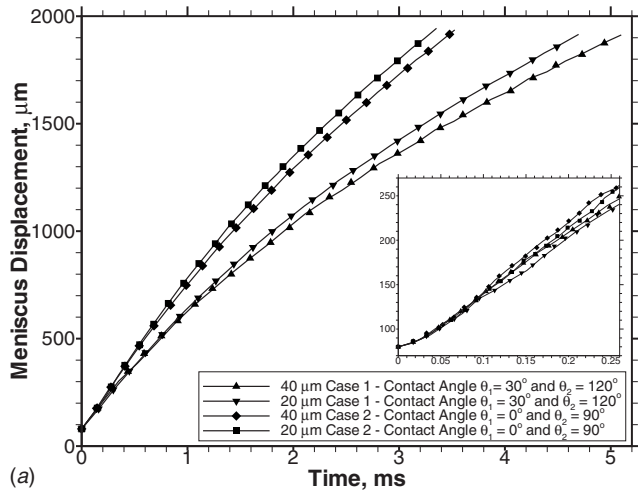


(b)

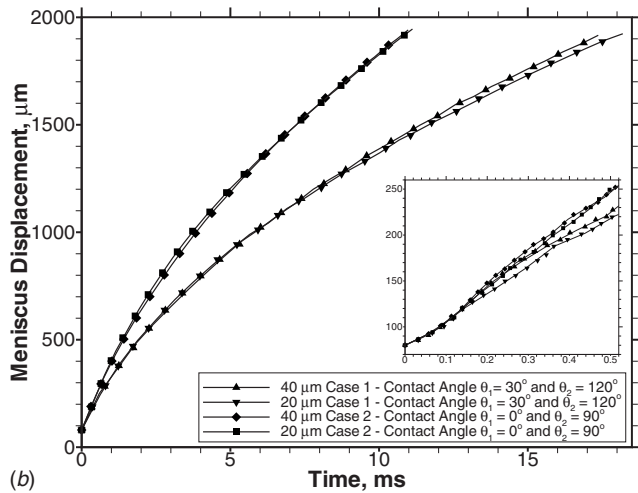
Fig. 7 The variation of meniscus stretch with liquid volume fraction for a nonpatterned microchannel for two different working fluids: (a) DI water and (b) ethanol

by controlling the size of the patterned surface. Such phenomena will find applications for performing biological reactions in microfluidic devices using the capillary flow. All biological reactions need sufficient incubation time to complete the reaction. It is believed that sufficient incubation time necessary for reaction to proceed will be inherently available in the patterned microchannel. The biological fluid will come in contact with surface, which will alternately assist and retard its flow. The region where the flow is retarded can be used for the reaction zone.

4.6 Variation of Meniscus Maximum, Average, and Centerline Velocity. The maximum, average, and centerline velocity of the meniscus is observed to show very high degree of fluctuations for all the cases and their magnitude decreases with time. The meniscus root mean squared (rms) velocities are computed and is provided in Table 4 for comparison purpose. It is found that the maximum velocity with DI water occurs for Case 2, followed by Case 1. Similar trends are observed with ethanol with a lower value in its magnitude. The frequency of fluctuations is observed to be higher with ethanol compared with DI water. It is observed that the pattern size and the surface condition on the bottom wall influence the rms velocity. The rms velocity for 20 μm patterned wall is higher compared with 40 μm patterned wall for all the cases with DI water and ethanol. Figure 12 shows the meniscus displacement with time of the contact line on the top and bottom walls with DI water (contact angles $\theta_1=30$ deg and θ_2



(a)



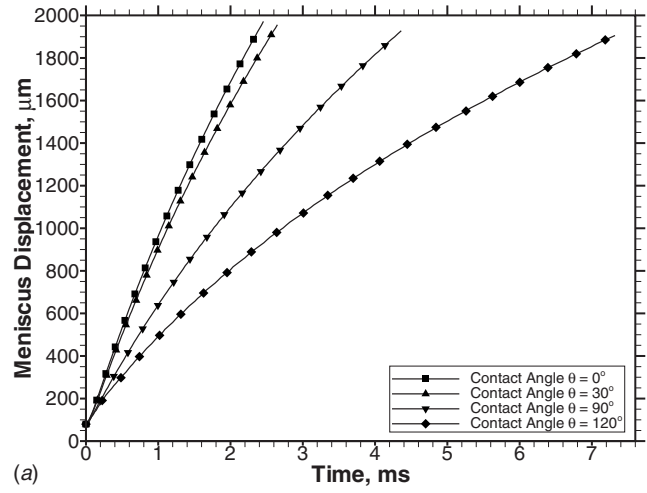
(b)

Fig. 8 The position of capillary meniscus with time for Cases 1 and 2 for two different working fluids: (a) DI water and (b) ethanol

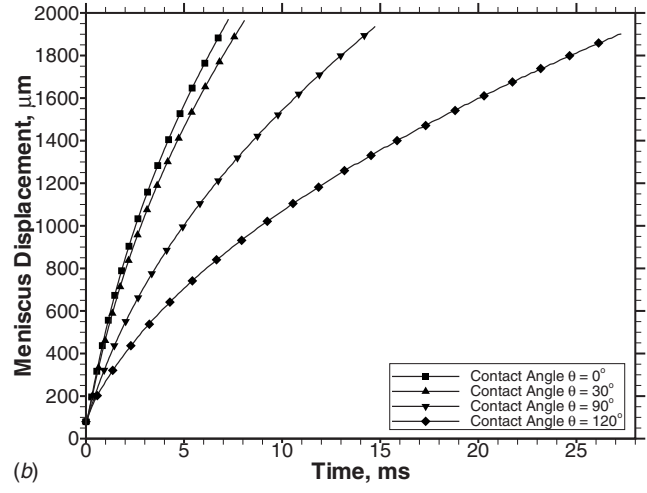
=120 deg) for 20 μm patterned microchannel. As the top and bottom contact lines of the meniscus show different displacement profiles, the velocity difference of the top and bottom contact line motions is also plotted in Fig. 12. The hydrophilic and hydrophobic regions have been marked in the plot. It is observed that difference in velocity increases/decreases and fluctuates with time due to the presence of alternate patterns. In the hydrophilic region, the top and bottom wall velocity difference is observed to decrease, whereas the same increases in the hydrophobic region. This presents an excellent opportunity for applications in microfluidic devices, which requires enhanced mixing for fluid delivery. This will also help in innovative design of capillary driven microfluidic devices.

Table 3 Meniscus position in micrometers from the channel inlet at 1 ms

Liquid	Case	40 μm alternate pattern	20 μm alternate pattern
DI water	Case 1	604.91	626.37
	Case 2	743.77	772.80
Ethanol	Case 1	320.11	319.39
	Case 2	388.21	396.41



(a)



(b)

Fig. 9 The position of capillary meniscus with time for a non-patterned microchannel for two different working fluids: (a) DI water and (b) ethanol

4.7 Effect of Large Pattern Sizes. Simulations are also performed considering 60 μm , 80 μm , and 100 μm patterns for DI water and ethanol to investigate the effect of larger pattern sizes. A dimensionless pattern size is defined (which is a ratio of pattern

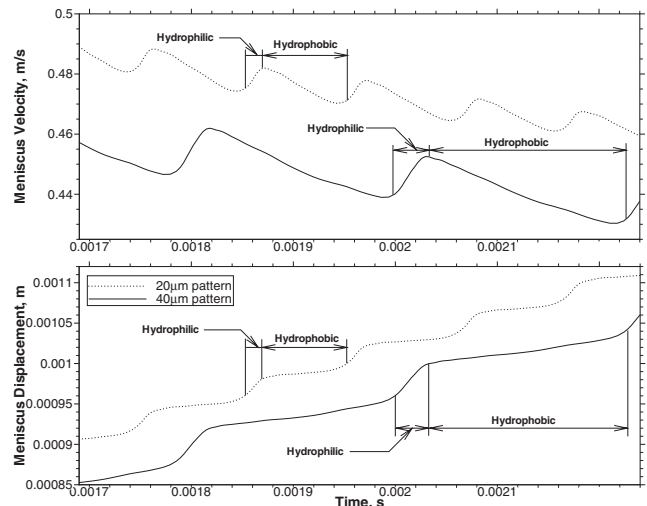


Fig. 10 Meniscus displacement of the capillary with time on the bottom wall with DI water (contact angles $\theta_1=30$ deg and $\theta_2=120$ deg) for 20 μm and 40 μm patterned microchannels

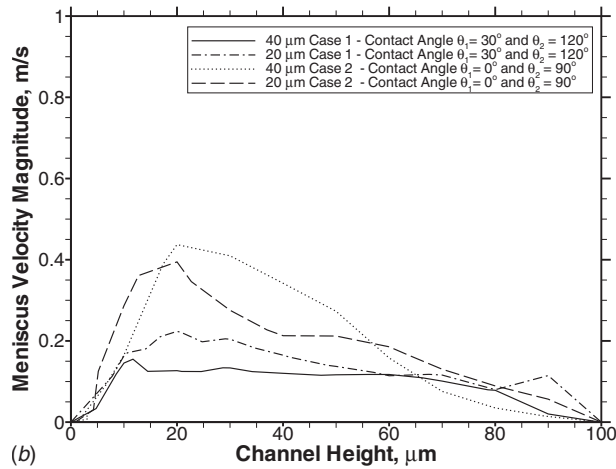
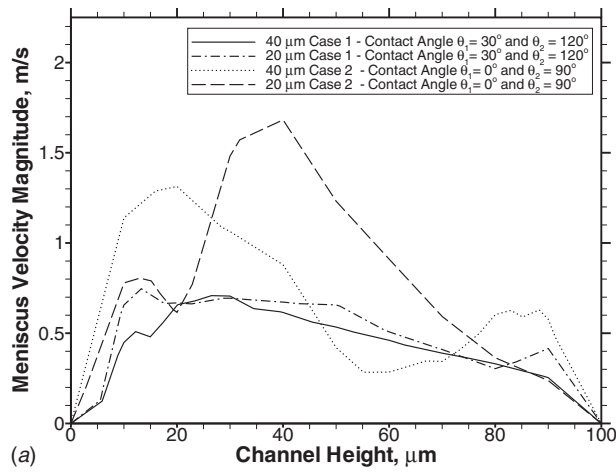


Fig. 11 Meniscus velocity distribution along the channel height for Cases 1 and 2 for two different working fluids: (a) DI water and (b) ethanol

size and microchannel height) here, for comparing the predicted results. Figure 13 shows the meniscus average velocity difference at top and bottom walls with dimensionless pattern size.

It is observed that, in the case of DI water with hydrophilic-hydrophobic pattern, the meniscus average velocity difference at top and bottom walls increases for a dimensionless pattern size of 0.6 and thereafter it decreases with the increase in pattern size. Whereas, for ethanol, the meniscus average velocity difference increases slightly with dimensionless pattern size and its magnitude is lower than that for DI water. It is to be noted that the top and bottom wall meniscus average velocity difference is related to meniscus stretch. With DI water as the working fluid, the meniscus stretch decreases as the pattern size is increased beyond 60 μm . However, in the case of hydrophilic-neutral pattern, the meniscus average velocity difference is observed to decrease with the increase in dimensionless pattern size for both DI water and

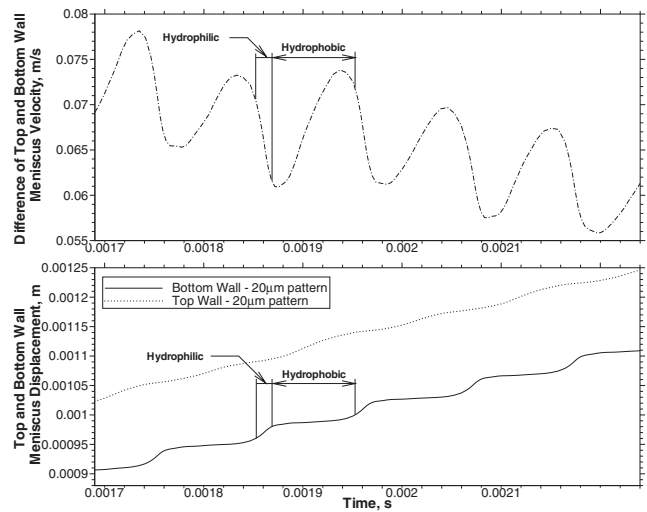


Fig. 12 Meniscus displacement of the capillary with time on the top and bottom wall with DI water (contact angles $\theta_1 = 30$ deg and $\theta_2 = 120$ deg) for 20 μm patterned microchannel

ethanol. The above results may be useful to optimize the design of a patterned microchannel for a given application.

4.8 Grid Issues. Simulations are also conducted to study the influence of grid resolution on the numerical solution. The simulation time for 10×200 grid cells is typically around 45 min on a 2.4 GHz AMD 64 Opteron processor running Linux with an access to 4 Gbyte RAM. It is to be noted that with the increase in the grid resolution in every direction by a factor of 2, the calculation time in a two-dimensional grid increases by a factor of 8. Also, the time step under such condition needs to be decreased by a factor of 2 in order to fulfill the CFL stability criteria. The grid cells are taken as square element as per the requirement of the VOF module.

The grid convergence of the solution has been tested by imposing different inlet boundary conditions, viz., pressure inlet (zero/positive), constant velocity inlet, and time varying velocity inlet using 10×200 , 12×240 , 14×280 , 20×400 , and 40×800 grid cells. It is to be noted that, when velocity inlet boundary conditions are imposed (Fig. 14(a) and 14(b)), the meniscus displacement curves do not show any amount of error for all the grid sizes considered. However, when the pressure inlet boundary condition is imposed (Fig. 15(a)), an error of about 2% is observed in meniscus displacement (less than 20 μm when the microchannel is half filled) as the grid is refined. The error reduces to about 1.5% when a positive pressure of 1000 N/m^2 inlet boundary condition is imposed (Fig. 15(b)). Raessi et al. [28] showed that there may be errors in interface normal vectors and curvatures at high grid resolutions when modeling surface tensions. This could result in overestimating the contact angle at high grid resolutions, which tend to decrease the meniscus displacement. Hence, for capillary driven studies where the filling time and meniscus displacement

Table 4 Meniscus rms velocity

Liquid	Case	40 μm alternate pattern			20 μm alternate pattern		
		Maximum	Average	Centerline	Maximum	Average	Centerline
DI water	Case 1	1.0722	0.4793	0.6292	1.1034	0.5063	0.6531
	Case 2	1.4454	0.6119	0.7775	1.5628	0.6644	0.8174
Ethanol	Case 1	0.3246	0.1507	0.2047	0.3339	0.1517	0.1956
	Case 2	0.4569	0.2020	0.2545	0.4825	0.2065	0.2562

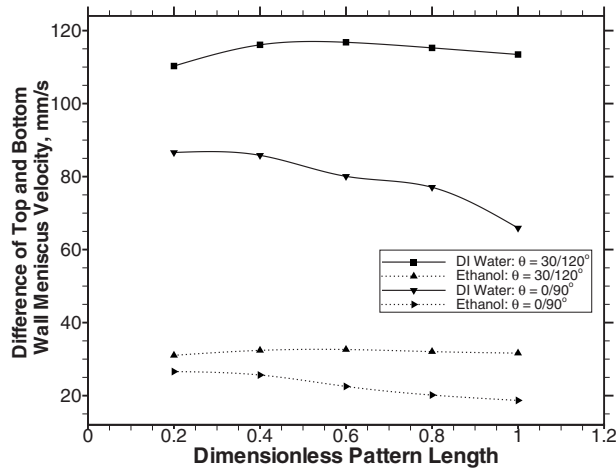


Fig. 13 Meniscus average velocity difference of top and bottom walls with dimensionless pattern size for DI water and ethanol

are important variables, it is preferable to use fewer grid nodes for simulations [7,9,12,29,13].

To study grid independence with respect to flow field variables, three simulations have been done using 2000, 2880, and 3920 grid cells. In Fig. 16, it is shown that the numerical results of total pressure and velocity magnitude as function of liquid volume

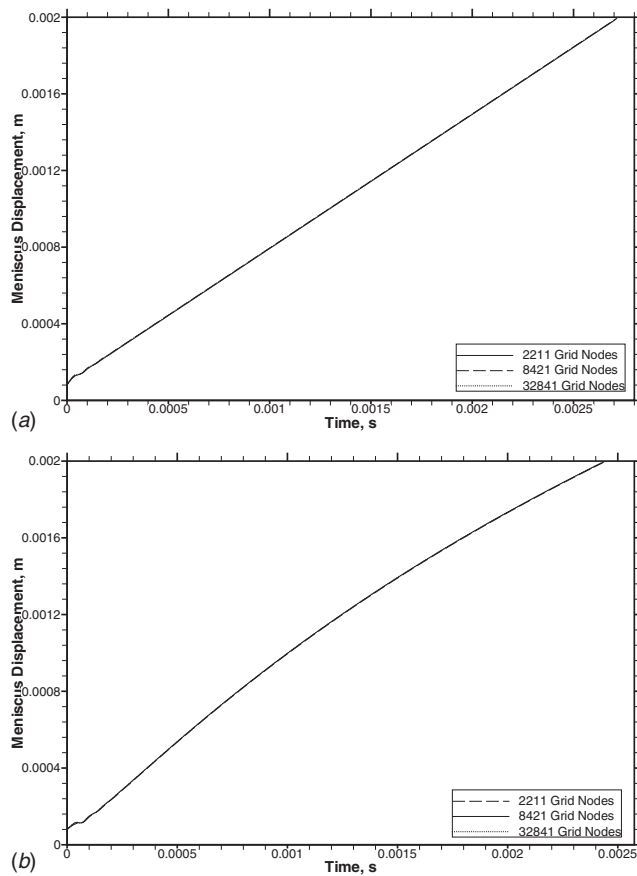


Fig. 14 Comparison of the position of the capillary meniscus with time for nonpatterned microchannel with DI water (contact angle $\theta=30$ deg) for different velocity inlet boundary conditions with different grid sizes: (a) velocity inlet=constant and (b) velocity inlet=time varying

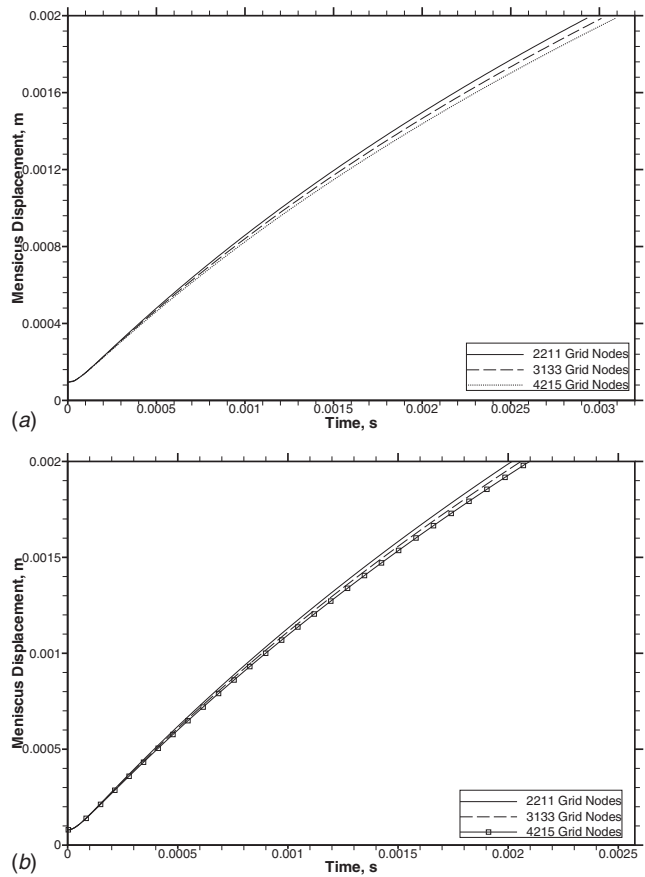


Fig. 15 Comparison of the position of the capillary meniscus with time for nonpatterned microchannel with DI water (contact angle $\theta=30$ deg) for different pressure inlet boundary conditions with different grid sizes: (a) pressure=0 N/m² and (b) pressure=1000 N/m²

fraction, with the coarsest of these three grids, are grid independent. The difference in the flow field variables are within 1.5% and 2.0%, respectively.

To check time-step independence, 2000 total grid cells (2211 nodes) are used and the simulations are executed for three time

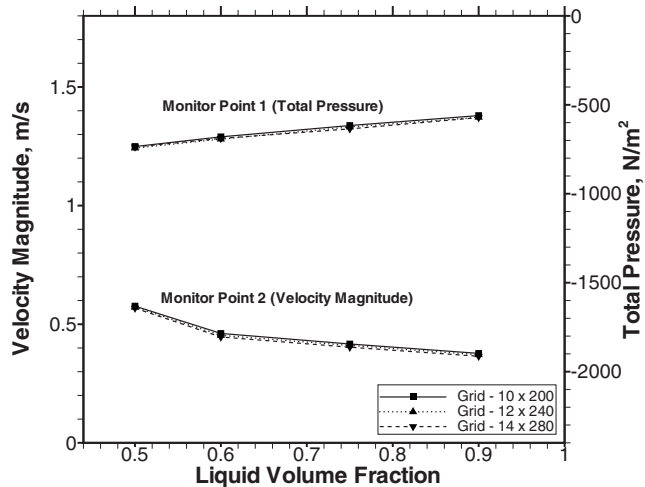


Fig. 16 Comparison of flow field variables with liquid volume fraction for nonpatterned microchannel with DI water (contact angle $\theta=30$ deg) with different grid sizes

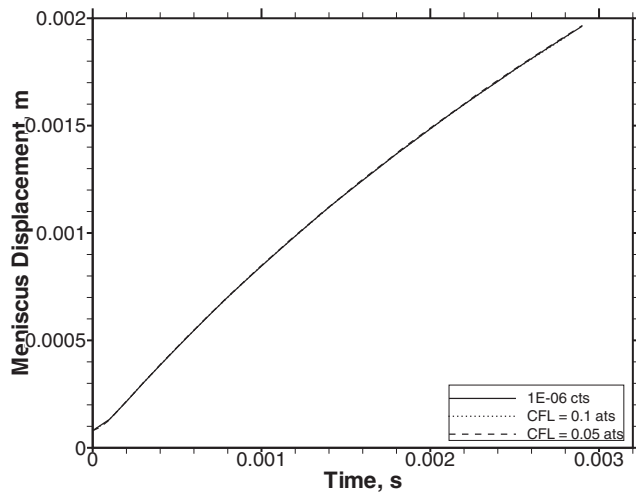


Fig. 17 Comparison of the position of the capillary meniscus with time for nonpatterned microchannel with DI water (contact angle $\theta=30$ deg) with different time-step sizes

steps— 1×10^{-6} s constant time step (cts), 0.1 CFL automatic time step (ats), and 0.05 CFL automatic time step (ats). In Fig. 17, it is shown that the results are time-step independent with 0.1 CFL automatic time step.

Figure 18 shows the profile of the capillary meniscus when the microchannel is half filled, with the three different grid sizes. It is observed that the meniscus interface is resolved well for all the grid sizes. The maximum difference of the term $[(\sqrt{x_{ic}^2 + y_{ic}^2})_{coarse} - (\sqrt{x_{ic}^2 + y_{ic}^2})_{fine}] / (\sqrt{x_{ic}^2 + y_{ic}^2})_{fine}$ was within 0.30%, where the values x_{ic} and y_{ic} denote the x and y components of the meniscus interface coordinates. Hence, a minimum of ten grid cells across the microchannel height is found to be adequate for the resolution of the meniscus interface. It is also found that by using different space discretization schemes (viz., first-order, second-order, and smart), insignificant deviation is observed in the predicted meniscus front.

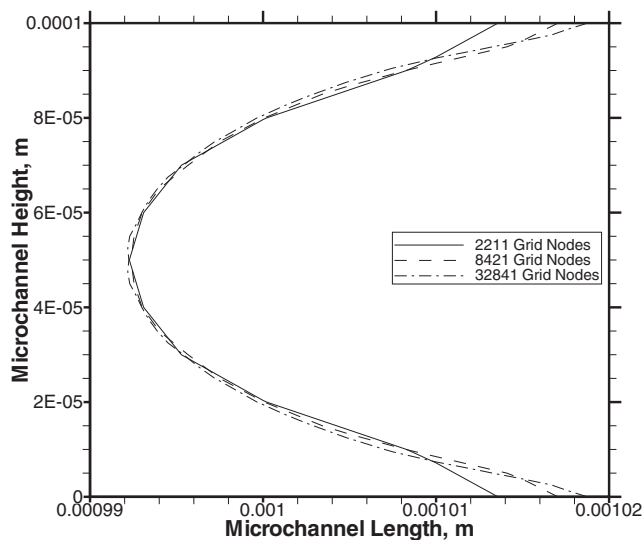


Fig. 18 Comparison of the profile of the capillary meniscus for nonpatterned microchannel with DI water (contact angle $\theta=30$ deg) at different grid resolutions when the microchannel is half filled

5 Conclusions

A two-dimensional numerical simulation of flow through a patterned microchannel has been carried out. Two different cases—alternate hydrophilic-hydrophobic bottom wall with contact angle 30 deg and 120 deg, respectively, and alternate hydrophilic-neutral bottom wall with contact angle 0 deg and 90 deg, respectively—are considered here. The pattern size is varied between 20 μm and 40 μm for each case. The volume of fluid method is used for simulating the free surface flow in the microchannel. Meniscus profiles with varying amplitude and shapes are obtained under the different specified surface conditions. Non-symmetric meniscus profiles are obtained by changing the contact angles of the hydrophilic and hydrophobic surfaces. The meniscus stretch is observed to fluctuate with time. Smaller pattern size produces enhanced capillary effect with DI water, whereas no appreciable gain is observed for ethanol. It is found that the meniscus displacement for alternate hydrophilic-hydrophobic surface is lower compared with the hydrophilic-neutral surface and the initial transient response of the displacement varies significantly with the surface characteristics. It is observed that the meniscus displacement can be manipulated suitably by appropriate choice of the pattern size and the contact angle for a given working fluid. It is also found that the meniscus velocity magnitude is higher for DI water and the position of the maximum velocity varies considerably for all the cases. The rms velocity for 20 μm patterned wall is found to be higher compared with the 40 μm patterned wall. The flow variations increase in the microchannel as the fluid traverses alternately between hydrophilic and hydrophobic regions due to a sharp change in the meniscus curvature at the interface. The effect of the surface tension of the fluid is shown to have significant effect on the capillary motion. Such flow phenomena in the microchannel indicate that flow control is possible by patterning the channel walls for applications related to microfluidic devices. Simulations are also performed to investigate the effect of larger pattern sizes. The meniscus average velocity difference at the top and bottom walls increases for a dimensionless pattern size of 0.6 and thereafter it decreases with the increase in pattern size in the case of DI water with hydrophilic-hydrophobic pattern. The design of a patterned microchannel may be optimized for a given application.

Acknowledgment

The support of Suman Mashruwala Advanced Microengineering Laboratory, IIT Bombay is highly appreciated.

Nomenclature

- Bo = Bond number
- Ca = Capillary number
- F = liquid volume fraction
- \mathbf{F}_s = volumetric force representing the surface tension
- h = channel height, local cell dimension
- L = distance traveled by liquid meniscus
- l = channel length
- \mathbf{n} = normal vector
- $\hat{\mathbf{n}}$ = unit vector normal to the surface
- $\hat{\mathbf{n}}_w$ = unit vector normal to the wall
- P = pressure
- R = radius of curvature
- t = time
- $\hat{\mathbf{t}}_w$ = unit vector tangent to the wall
- U = characteristic velocity
- u = velocity component in x -direction
- u_{avg} = average velocity
- \mathbf{V} = velocity vector
- v = interface velocity
- ρ = density of fluid

σ = surface tension of fluid
 θ = contact angle
 μ = viscosity of fluid
 κ = curvature of the surface

Subscripts

avg = average
 s = surface tension
 w = wall
 1 = gas phase
 2 = liquid phase

References

- [1] Madou, M., 2002, *Fundamentals of Microfabrication*, CRC, New York.
- [2] Deval, J., Umali, T. A., Lan, E. H., Dunn, B., and Ho, C. M., 2004, "Reconfigurable Hydrophobic/Hydrophilic Surfaces in Microelectromechanical Systems (MEMS)," *J. Micromech. Microeng.*, **14**, pp. 91–95.
- [3] Zhao, B., Jeffrey, M. S., and Beebe, D. J., 2001, "Surface-Directed Liquid Flow Inside Microchannels," *Science*, **291**, pp. 1023–1026.
- [4] Kim, D. S., Lee, K. C., Kwon, T. H., and Lee, S. S., 2002, "Microchannel Filling Flow Considering Surface Tension Effect," *J. Micromech. Microeng.*, **12**, pp. 236–246.
- [5] Yang, L. J., Yao, T. J., and Tai, Y. C., 2004, "The Marching Velocity of the Capillary Meniscus in a Microchannel," *J. Micromech. Microeng.*, **14**, pp. 220–225.
- [6] Salamon, T., Lee, W., Krupenkin, M., Hodes, M., and Kolodner, P., 2005, "Numerical Simulation of Fluid Flow in Microchannels With Superhydrophobic Walls," International Mechanical Engineering Conference and Exposition, Paper No. 82641.
- [7] Byun, D., Budiono, Yang, J. H., Lee, C., and Lim, K. W., 2005, "Numerical Visualization of Flow Instability in Microchannel Considering Surface Wettability," Second International Conference on Fuzzy Systems and Knowledge Discovery, Paper No. LNAI 3613.
- [8] Dalton, T., Eason, C., Enright, R., Hodes, M., Kolodner, P., and Krupenkin, T., 2006, "Challenges in Using Nano Textured Surfaces to Reduce Pressure Drop Through Microchannels," Seventh International Conference on Thermal, Mechanical and Multiphysics Simulation and Experiments in Micro-Electronics and Micro-Systems, pp. 1–3.
- [9] Yang, H. Q., and Przekwas, A. J., 1998, "Computational Modeling of Microfluid Devices With Free Surface Liquid Handling," First International Conference on Modeling and Simulation of Microsystems, pp. 498–505.
- [10] Hirt, C. W., and Nichols, B. D., 1981, "Volume of Fluid (VOF) Method for the Dynamics of Free Boundaries," *J. Comput. Phys.*, **39**, pp. 201–225.
- [11] Kothe, D. B., Rider, W. J., Mosso, S. J., and Brock, J. S., 1996, "Volume Tracking of Interfaces Having Surface Tension in Two and Three Dimensions," AIAA Paper No. 96-0859.
- [12] Saha, A. A., Mitra, S. K., Tweedie, M., Roy, S., and McLaughlin, J., 2008, "Experimental and Numerical Investigation of Capillary Flow in SU8 and PDMS Microchannels With Integrated Pillars," *Microfluid. Nanofluid.*
- [13] Huang, W., Liu, Q., and Li, Y., 2006, "Capillary Filling Flows Inside Patterned-Surface Microchannels," *Chem. Eng. Technol.*, **29**, pp. 716–723.
- [14] Nayak, K., Kulkarni, P. D., Deepu, A., Sitaraman, V. R., Punidha, S., Saha, A. A., Ravikanth, M., Mitra, S. K., Mukherji, S., and Rao, V. R., 2007, "Patterned Microfluidic Channels Using Self-Assembled Hydroxy-Phenyl Porphyrin Monolayer," Seventh IEEE International Conference on Nanotechnology, Paper No. 404, pp. 238–240.
- [15] Probstein, R. F., 1994, *Physicochemical Hydrodynamics*, Wiley, New York.
- [16] Patankar, S., 1980, *Numerical Heat Transfer and Fluid Flow*, Hemisphere, New York.
- [17] Brackbill, J. U., Kothe, D. B., and Zemach, C., 1992, "A Continuum Method for Modeling Surface Tension," *J. Comput. Phys.*, **100**, pp. 335–354.
- [18] Rosengarten, G., Harvie, D. J. E., and White, J. C., 2006, "Contact Angle Effects on Microdroplet Deformation Using CFD," *Appl. Math. Model.*, **30**, pp. 1033–1042.
- [19] Washburn, E. W., 1921, "The Dynamics of Capillary Flow," *Phys. Rev.*, **17**, pp. 273–299.
- [20] Zeng, J., 2007, "On Modeling of Capillary Filling," http://www.coventor.com/pdfs/on_modeling_of_capillary_filling.pdf.
- [21] Ralston, J., Popescu, M., and Sedev, R., 2008, "Dynamics of Wetting from an Experimental Point of View," *Annu. Rev. Mater. Res.*, **38**, pp. 23–43.
- [22] Dussan, E. B., 1979, "On the Spreading of Liquids on Solid Surfaces: Static and Dynamic Contact Angles," *Annu. Rev. Fluid Mech.*, **11**, pp. 371–400.
- [23] de Gennes, P. G., 1985, "Wetting: Statics and Dynamics," *Rev. Mod. Phys.*, **57**, pp. 827–890.
- [24] Blake, T. D., 2006, "The Physics of Moving Wetting Lines," *J. Colloid Interface Sci.*, **299**, pp. 1–13.
- [25] ESI CFD Inc., 2007, *CFD-ACE+ Software Manuals*, V2007.2.
- [26] Stange, M., Dreyer, M. E., and Rath, H. J., 2003, "Capillary Driven Flow in Circular Cylindrical Tubes," *Phys. Fluids*, **15**, pp. 2587–2601.
- [27] Dreyer, M. E., Delgado, A., and Rath, H. J., 1994, "Capillary Rise of Liquid Between Parallel Plates Under Microgravity," *J. Colloid Interface Sci.*, **163**, pp. 158–168.
- [28] Raessi, M., Mostaghimi, J., and Bussmann, M., 2007, "Advecting Normal Vectors: A New Method for Calculating Interface Normals and Curvatures When Modeling Two Phase Flows," *J. Comput. Phys.*, **226**, pp. 774–797.
- [29] Trutschel, R., and Schellenberger, U., 1998, "Dynamic Simulation of Free Surfaces in Capillaries With the Finite Element Method," *Int. J. Numer. Methods Fluids*, **26**, pp. 485–495.
- [30] Yang, A. S., 2008, "Investigation of Liquid-Gas Interfacial Shapes in Reduced Gravitational Environments," *Int. J. Mech. Sci.*, **50**, pp. 1304–1315.